Full length article

Phase-field modeling of reactive wetting and growth of the intermetallic Al₂Au phase in the Al-Au system

Fei Wang [a, b, *], Andreas Reiter [b], Michael Kellner [a, b], Jürgen Brillo [c], Michael Selzer [a, b], Britta Nestler [a, b, **]

[a] Institute of Materials and Processes, Karlsruhe University of Applied Sciences, Moltkestrasse 30, 76133 Karlsruhe, Germany
[b] Institute of Applied Materials, Karlsruhe Institute of Technology, Straße am Forum 7, 76131 Karlsruhe, Germany
[c] Institut für Materialphysik im Weltraum, Deutsches Zentrum für Luft- und Raumfahrt (DLR), 51170 Köln, Germany

ABSTRACT

When an Al-droplet is in contact with an Au-solid substrate, the liquid phase reacts with the substrate and an intermetallic layer is formed at the solid-liquid interface due to diffusion and reaction. This phenomenon has been commonly observed in the soldering process and the wetting is termed as reactive wetting, in contrast to the inert wetting where the droplet does not react with the base materials and the substrate is flat. Young's law can be used to interpret the contact angle in the static state, but is not able to predict the dynamics in the process of reactive wetting. In this work, we present a multi-phase model including phase transition and fluid dynamics to investigate the effect of the formation of the intermetallic Al₂Au phase and capillary flow on the reactive wetting in the Al-Au system. In order to capture phase boundaries of solid-, liquid- and intermetallic-vapor, phase-field simulations are performed based on a ternary (Al-Au-X) phase diagram concept and using experimental data. It has been found that the increase of both the liquid-intermetallic interfacial tension as well as the capillary flow lead to an inhibition effect for the growth of the intermetallic phase.

© 2017 Acta Materialia Inc. Published by Elsevier Ltd. All rights reserved.

1. Introduction

In the process of soldering, the liquid solder spreads on the solid substrate and wets the base materials. The wettability of the solder on the substrate can be in principle understood by considering a three-phase equilibrium at the triple line according to Young's law [1]. In contrast to the considerations of non-reactive systems in Young's equation, the solder wire sometimes chemically reacts with the base materials and an intermetallic layer is spontaneously formed in between the solder and the base materials [2–4]. Because of the formation of the intermetallic phase, the wettability of the system may be weakened or improved. In the present study, we take Al-Au as an exemplary system because of its outstanding anti-oxidation property and excellent conductivity, and consider the effect of the formation of the intermetallic Al₂Au phase on the reactive wetting of the system.

Presently, for the study of reactive wetting, an Al droplet on top of an Au substrate is considered. As sketched in Fig. 1, the reactive wetting during soldering is an intricate process which involves diffusion, reaction and convection, and may be divided into four stages. A similar sketch is shown in a previous work [5], but fluid dynamics is not considered therein. In stage I, the droplet spreads on the surface of the substrate to approach the equilibrium state where the contact angle ϑ between the droplet and the substrate at the triple junction, according to Young's law, fulfills the relation: $\gamma_{LV}\cos\vartheta + \gamma_{SV} = \gamma_{LS}$. Here, γ_{ij} stands for the surface/interfacial tension of the i-j surface/interface and refers to L = liquid, V = vapor and S = solid substrate. The difference of the spreading in stage I from the consideration of Young's equation is, that with time, the solid substrate dissolves into the droplet because the solid-liquid interface is thermodynamically unstable according to the phase equilibrium in the phase diagram [6]. The dissolution rate depends on the thermodynamic and kinetic parameters. In stage II,

* Corresponding author. Institute of Materials and Processes, Karlsruhe University of Applied Sciences, Moltkestrasse 30, 76133 Karlsruhe, Germany: Institute of Applied Materials,Karlsruhe Institute of Technology, Straße am Forum 7, 76131 Karlsruhe, Germany.
** Corresponding author. Institute of Materials and Processes, Karlsruhe University of Applied Sciences, Moltkestrasse 30, 76133 Karlsruhe, Germany: Institute of Applied Materials,Karlsruhe Institute of Technology, Straße am Forum 7, 76131 Karlsruhe, Germany.
E-mail addresses: fei.wang@kit.edu (F. Wang), britta.nestler@kit.edu (B. Nestler).
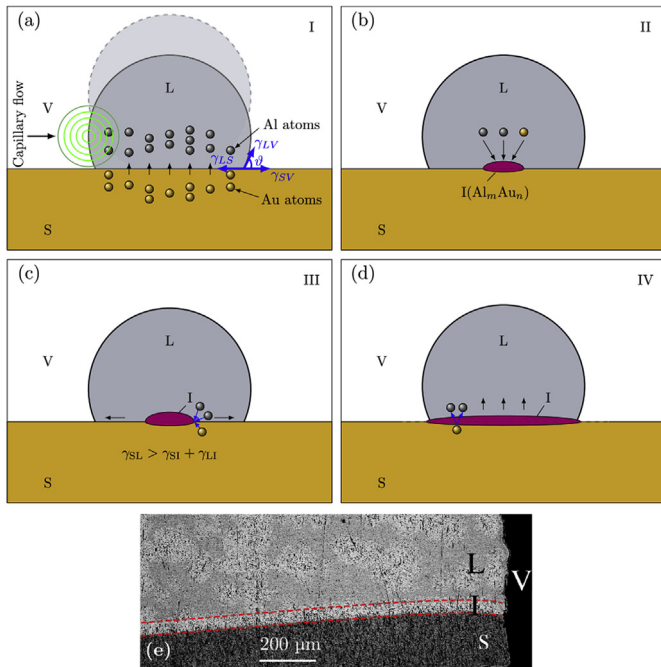
Fig. 1. Sketch of the four stages for reactive wetting when an Al droplet is placed on top of an Au substrate (a)–(d): In stage I, the droplet spreads on the substrate to form a contact angle ϑ and meanwhile the substrate dissolves into the liquid phase by diffusion. In stage II, an intermetallic phase Al_mAu_n nucleates at the S-L interface. In stage III, the intermetallic phase spreads in the horizontal direction due to diffusion and the surface tension relation: $\gamma_{SL} > \gamma_{SI} + \gamma_{LI}$. In stage IV, the intermetallic phase increases its thickness with time which is achieved by the diffusion of the Au atoms into the liquid phase passing through the intermetallic phase. Here, the following notations are used: L: liquid phase, S: solid phase, V: vapor, I: intermetallic phase. Figures (a)–(d) are adapted from our previous work [5]. The difference is that capillary flow caused by the capillary force, which is not considered in Ref. [5], is presently incorporated, as illustrated by the green circles in the stage I. The capillary flow not only affects the spreading of the S-L-V triple junction in the stage I but also influences the movement of the S-I-V and L-I-V triple junctions when the stage transits from III to IV. (e) is an experimental microstructure showing the formation of an intermetallic layer in between the Al-liquid droplet and the Au-solid substrate. The microstructure is obtained by a sessile droplet experiment [13]. (For interpretation of the references to color in this figure legend, the reader is referred to the Web version of this article.)

the aluminum and gold atoms combine with a ratio of $m:n$, forming a nucleus of Al_mAu_n at the solid-liquid interface. Which intermetallic phase is energetically favorable depends upon the difference of the effective heat of formation [7]: $\Delta H = \Delta H_{Al_mAu_n} - (m\Delta H_{Al} + n\Delta H_{Au})$. Although a single nucleus is schematically illustrated in Fig. 1, a number of nuclei may actually form at the S-L interface. In stage III, the intermetallic phase spreads in the lateral direction due to a diffusion driven phase transformation which is caused by the concentration gradient in the intermetallic phase as well as by the surface tension relation [8]: $\gamma_{SL} > \gamma_{SI} + \gamma_{LI}$, where I denotes the intermetallic phase. Due to the surface tension relation, the S-L-I triple junction is not stable inside the droplet and the intermetallic phase grows in the lateral direction until it is in contact with the surrounding vapor phase. After stage III, the L-S interface is completely covered by the intermetallic layer. In stage IV, the thickness of the intermetallic layer increases with time and the growth mechanism is diffusion and reaction. Since Au is the predominant diffusant in the Al-Au system [9], the Au atoms diffuse through the bulk of the intermetallic layer and chemically react with Al atoms at the L-I interface, resulting in the thickening of the intermetallic layer. The change of the thickness d with time t follows the empirical expression [10–12]: $d \sim t^n$, $1/3 \leq n \leq 1$. An experimental microstructure showing that the Al-

liquid droplet and the Au-solid substrate are completely separated by an intermetallic layer is illustrated in Fig. 1 (e). The experimental microstructure is obtained by a sessile droplet experiment, which is described in detail in Ref. [13].

Since the droplet reacts with the base materials, the substrate is not planar, and hence Young's law (which assumes a flat substrate) is not applicable. As experimentally noticed [14,15], the dynamics of the contact angle in the case of reactive wetting behave differently from inert wetting. Aksay et al. [16] and Laurent et al. [17] proposed that the contact angle due to reaction is expressed as $\cos\vartheta = \cos\vartheta^0 + (\gamma_{SL} - \gamma_{SL}^0)/\gamma_{LV} - \Delta F/\gamma_{LV}$, where ϑ^0 is the contact angle without reaction as given by Young's law, γ_{SL} and γ_{SL}^0 are the interfacial tensions between the liquid and the solid after and before the reaction, respectively, and ΔF is the change of the free energy due to reaction. This relation has been widely employed to interpret the contact angle in the process of reactive wetting [14,18–20]. One unsatisfactory point of this relation is that it makes no sense to discuss the S-L interfacial tension after stage III where the solid-liquid interface is completely covered by the intermetallic layer. Another flaw is that this relation is derived based on the Young's equation which is for a static scenario and may not be used for a dynamic situation like reactive wetting. It has been shown [21,22] that the evolution of the contact angle in the process of reactive wetting follows an exponential form: $\vartheta - \vartheta_e \sim \exp(-t/\chi)$, where ϑ_e is the equilibrium contact angle and χ is the characteristic time. After a sufficiently long time, the contact angle converges to the equilibrium value ϑ_e, which is obtained by considering the equilibrium condition at the L-I-V triple junction [19,23], rather than the non-existing equilibrium at the L-S-V triple point.

In contrast to the classic sharp interface model, the phase-field model is a general diffuse-interface method to investigate different mechanisms of phase transition [24,25]. This method has been successfully applied to the studies of reactive wetting (see Refs. [8,26,27,29–32]). In the literature, there are two types of phase-field methods to model the reactive system. In the first type, the system is considered to consist of three phases: solid, liquid and vapor, and two components. Here, the solid and fluid phases (liquid and vapor) are distinguished by the phase-field order parameter. The liquid and vapor phases are modeled by a double well potential and are characterized by the mass density of each component. In this treatment, the gradient energy contribution from the phase-field and the mass density are included and the model is in fact a combination of the Allen-Cahn model with the Cahn-Hilliard diffusion equation. This type of phase-field model has been used by Wheeler et al. [31] for reactive wetting and by other researchers for other applications [33,34]. In the second type, the system is considered to comprise three phases: solid, liquid and vapor, and three components: A, B and X, where A and B are metal elements of a binary alloy and X is the main component of the vapor. In this model, the gradient energy contribution from the concentration has not been included and all the phases are characterized by the phase-field order parameter. This model is in fact a coupling of the Allen-Cahn model with the normal diffusion equation (not Cahn-Hilliard). A key point of this model is that a ternary A-B-X phase diagram has to be extended from the binary A-B phase diagram in order to model the phase-boundaries and the phase equilibria of L-V, S-V and I-V. This type of model has been originally used by Villanueva et al. [30] for reactive wetting and by other researchers for other applications [35].

The second type of the phase-field model is applied in the present work. As aforementioned, in the reactive wetting process, intermetallic phases usually form between the liquid and the substrate. The presence of intermetallic phases has not been addressed in the phase-field studies of Wheeler et al. [31] and

Villanueva et al. [30], until a subsequent work of Villanueva et al. [8]. However, the ternary phase diagram in the work of Villanueva et al. [8] seems not to be correlated to a realistic binary system. In the current work, we present a phase-field model incorporating diffusion, reaction and convection to investigate the reactive wetting process with the formation of the intermetallic Al_2Au phase in the Al-Au system. The ternary-component concept of Villanueva et al. [8] is herein adopted in order to capture all occurring phase boundaries of L-V, I-V and S-V. In particular, we will attempt to link the constructed phase diagram of four phases: solid, liquid, intermetallic and vapor for the three components: Al, Au and X as close as possible to the realistic binary phase diagram of Al-Au [36].

In the mentioned phase-field models, the fluid velocity is computed in both the solid and fluid phases, but the viscosity of the solid phase is set to be at least 5 orders higher than that of the fluid phases. In fact, the solid phase is supposed to be non-advective and the convection in the solid can be neglected as long as the no-slip boundary condition at the solid-fluid interface is able to be achieved. Based on a recent work in our group [37] which is developed from the work of Beckermann et al. [38], we will introduce an alternative multiphase and multicomponent phase-field model for the investigation of reactive wetting. The way to model the fluid flow is different from previous works [8,29–31] and the present model is expected to be computationally cheaper than previous ones. Additionally, previous works are mostly conducted in 2D. In the current work, beside systematical studies in 2D, we will present selected 3D simulations as well as some geometric interpretations to show different evolution behavior of the contact angle in 2D and 3D and that the contact angle is even affected by the curvature,

introduced and the summation of the local volume fraction over all the phases is unity. As such, the volume fraction of the α-phase is one, i.e., $\varphi_\alpha = 1$, in the bulk α-phase and satisfies the relation, $0 < \varphi_\alpha < 1$, within the diffuse interface and is exactly zero in the other bulk phases. The time evolution of the phase-field order parameter is such as to minimize the free energy of the system. In contrast to the sharp interface model [28], a significant advantage of the phase-field model is that complex geometries for the interfaces are implicitly tracked. For more details of the phase-field approach and its applications, we refer to Refs. [39–41].

In this section, we present a multi-phase and multi-component phase-field model incorporating diffusion, reaction and convection. The coupling of the diffusion mechanism with the phase-field model is an extension of our previous work [5]. One significant difference of the present work from Ref. [5] is that fluid dynamics, which is not included in Ref. [5], is incorporated in the current phase-field model. Moreover, in contrast to the modeling of capillary flow by setting high viscosity ratio for solid and fluid phases (see Ref. [8] and the references therein), we propose an alternative approach for the modeling of capillary flow, based on a fluid dynamic model of Beckermann et al. [38].

2.1. The basic phase-field model incorporating the diffusion mechanism

The starting point for the phase-field model is the formulation of the free energy functional of the system, which is postulated as [25].

$$\mathscr{F}(\varphi, \mathbf{c}) = \int_V \left[\sum_\alpha f^\alpha(\mathbf{c}) \frac{h(\varphi_\alpha)}{\sum_{\beta=1}^N h(\varphi_\beta)} + \sum_\alpha^N \sum_{\beta > \alpha} \varepsilon \gamma_{\alpha\beta} \left| \varphi_\alpha \nabla \varphi_\beta - \varphi_\beta \nabla \varphi_\alpha \right|^2 \right.$$
$$\left. + \frac{16}{\pi^2} \sum_\alpha^N \sum_{\beta > \alpha} \frac{\gamma_{\alpha\beta}}{\varepsilon} \varphi_\alpha \varphi_\beta + \sum_\alpha^N \sum_{\beta > \alpha} \sum_{\delta > \beta} \gamma_{\alpha\beta\delta} \varphi_\alpha \varphi_\beta \varphi_\delta \right] dv, \tag{1}$$

which has not been addressed in Young's equation.

For the computation of fluid dynamics, experimental data for the temperature dependent density and viscosity are incorporated in the model formulation. The phase-field simulations reveal that the contact angle between the interfaces of the intermetallic layer exhibits an exponential growth behavior for large interfacial tensions of γ_{LI}, which is consistent with the aforementioned work. For small values of γ_{LI}, the angle first decreases and then increases with time. This evolution behavior is similar to the observation in the model of Aksay et el. [16], but due to a different mechanism. Furthermore, we shed light on the effect of capillary flow and the formation of the intermetallic phase on the dynamic behavior of the apparent contact angle of the droplet.

2. Phase-field approach

The used phase-field model [24,25] is a thermodynamic-principle-based model, where distinct phases are separated by a diffuse interface, in contrast to the conventional sharp interface with zero interfacial width. In this diffuse interface method, a vector of the phase-field order parameter $\varphi = (\varphi_\alpha, \varphi_\beta, \varphi_\gamma, \cdots)$ which denotes the corresponding volume fraction of $(\alpha, \beta, \gamma, \cdots)$ phases is

where V is the volume occupied by the system with N phases and K components, $\varphi = (\varphi_1, \varphi_2, \cdots, \varphi_N)$ and $\mathbf{c} = (c_1, c_2, \cdots, c_K)$ are, respectively, the vectors of the phase-field order parameter and the concentration. f^α is the concentration dependent bulk free energy density of phase α and $h(\varphi_\alpha)$ is an interpolation function which is chosen to be $h(\varphi_\alpha) = \varphi_\alpha(3 - 2\varphi_\alpha)$ satisfying the condition $h(1) = 1$ and $h(0) = 0$. A formulation of the bulk free energy density is given in section 3. ε is a length parameter determining the width of the diffuse interface and $\gamma_{\alpha\beta}$ is a modeling parameter which is related to the interfacial tension of the α-β interface.

In the free energy functional $\mathscr{F}(\varphi, \mathbf{c})$ of Eq. (1), we adopt an obstacle potential $\sim \varphi_\alpha \varphi_\beta$, in contrast to the double well potential $\sim \varphi_\alpha^2 \varphi_\beta^2$ in other phase-field models [8,29]. In the latter case, the diffuse interface follows a hyperbolic tangent function and the interfacial width is generally infinite large. In the former case, the diffuse interface is depicted by a sinusoidal function and the interface width is finite. Thus, by choosing the obstacle potential, the computational effort has been significantly reduced since the calculations are restricted to a finite diffuse interface, in contrast to the calculations within an infinite diffuse interface for the double well potential.

The time evolution of the order parameter φ_α is such as to reduce the free energy functional of the system and follows the Allen-Cahn equation [42].

$$\tau(\varphi)\varepsilon\frac{\partial\varphi_\alpha}{\partial t} = -\frac{\delta\mathscr{F}}{\delta\varphi_\alpha} - \mathscr{L}, \qquad (2)$$

where $\tau(\varphi) = \sum_\alpha\sum_\beta\tau_{\alpha\beta}\varphi_\alpha\varphi_\beta / \sum_\alpha\sum_\beta\varphi_\alpha\varphi_\beta$ is a relaxation parameter in which $\tau_{\alpha\beta}$ is related to the kinetic coefficient of the α-β interface, and $\mathscr{L}$ is the Lagrange multiplier ensuring the constraint that the summation of the local volume fraction φ_α over all the phases is unity, namely, $\sum_{\alpha=1}^N\varphi_\alpha = 1$. Here, the time derivative is defined in the material-fixed Lagrange coordinate.

In comparison with the sharp interface model, we clarify several concepts in the diffuse interface model. In the phase-field method, an α-β interface is given by the locus of $\varphi_\alpha = \varphi_\beta = 1/2$, an α-β-δ triple junction is defined as $\varphi_\alpha = \varphi_\beta = \varphi_\delta = 1/3$, and an α-β-δ-γ quadruple junction is given by $\varphi_\alpha = \varphi_\beta = \varphi_\delta = \varphi_\gamma = 1/4$. A modified marching square algorithm has been used to identify the interface and the contact angle at the triple junction. For readers who are interested in the algorithm for qualitative angle measurement in the phase-field model, we refer to Ref. [43].

The dynamics of the concentration are governed by the diffusion equation

$$\frac{\partial c_i}{\partial t} = -\nabla\cdot\mathbf{j}_i. \qquad (3)$$

Here, the diffusion flux $\mathbf{j}_i$ is expressed as $\mathbf{j}_i = -M_i\nabla\mu_i$, where the chemical potential μ_i is defined as $\mu_i := \partial_{c_i}f$ and the chemical potential gradients from other components are not considered. In comparison with Fick's law for the diffusion flux $\mathbf{j}_i = -D_i(\varphi)\nabla c_i$, the mobilities M_i are related to the diffusivities $D_i(\varphi)$ as $M_i = D_i(\varphi)/\partial_{c_i}\mu_i$. With the fact that $\partial_{c_i}\mu_i = R_gT/v_mc_i$ for ideal and regular solutions, the mobilities are further expressed as

$$M_i = \frac{v_m}{R_gT}D_i(\varphi)c_i, \qquad (4)$$

where v_m is the molar volume, R_g is the universal gas constant, $D_i(\varphi)$ is the diffusion coefficient which is interpolated as $D_i(\varphi) = \sum_{\alpha=1}^N D_i^\alpha h(\varphi_\alpha)$. Here, D_i^α is the self-diffusivity of the i-th component in the α phase.

To further derive a thermodynamically consistent diffusion flux, we employ the isothermal and isobaric Gibbs-Duhem equation: $\sum_{i=1}^K c_i\nabla\mu_i = 0$, which is a thermodynamic relation derived from the fundamental thermodynamic equation [44]. The Gibbs-Duhem equation is reformulated as $\nabla\mu_i = \sum_{j=1}^K(\delta_{ij} - c_j)\nabla\mu_j$, where δ_{ij} is the Kronecker delta. Thus, the diffusion equation is rearranged as

$$\frac{\partial c_i}{\partial t} = \nabla\cdot(\mathbf{L}\cdot\nabla\boldsymbol{\mu}), \qquad (5)$$

where the component L_{ij} of the matrix $\mathbf{L}\in\mathbb{R}^{K\times K}$ reads $L_{ij} := \frac{v_m}{R_gT}D_ic_i(\delta_{ij} - c_j)$ and the vector $\boldsymbol{\mu}$ is defined as $\boldsymbol{\mu} := (\mu_1, \cdots, \mu_K)^T\in\mathbb{R}^K$. It can be checked that the matrix $\mathbf{L}$ is symmetric and positive semi-define, which is consistent with Onsager's theorem [45]. It should be pointed that the cross-terms L_{ij} of the mobilities are not due to the diffusion potential gradients of other components j ($j\neq i$), but as a result of the Gibbs-Duhem equation. In comparison with Eq. (3), Eq. (5) is more thermodynamically consistent because of the coupling of the Gibbs-Duhem equation.

2.2. Modeling of the capillary flow

The coupling of Eq. (2) and Eq. (5) enables to model the process of reaction and diffusion. Yet, at liquid states the transfer of mass consists of another contribution from convection for fluids with a velocity of $\mathbf{u}$. Taking convection into account, the evolution equations for the concentrations are expressed as [8].

$$\frac{\partial c_i}{\partial t} + \mathbf{u}\cdot\nabla c_i = \nabla\cdot\sum_j L_{ij}(\varphi, \mathbf{c})\nabla\mu_j, \qquad (6)$$

where the incompressibility condition $\nabla\cdot\mathbf{u} = 0$ has been used to simplify the convective part, namely, $\nabla\cdot(\mathbf{u}c_i) = c_i\nabla\cdot\mathbf{u} + \mathbf{u}\cdot\nabla c_i$. Incorporating the advective term into the phase-field equations requires some additional modifications due to the presence of the solid phases, as those are not supposed to experience any advection. For a solid-liquid interface, this requires setting the advective term to zero for both phases, since the Lagrange multiplier due to the sum-constraint will otherwise lead to an advection of both phases with approximately half the velocity. As for the obstacle potential the phase-field values in the bulk are constant, this does not have any detrimental effect on the advection within a bulk liquid region. The same principle can be applied in the general case as long as there is only a single liquid phase present. When at least two liquid phases are present at a given point, an advective interaction between them needs to be allowed, while it is still desirable to keep the solid phases fixed. A simple way of (approximately) fulfilling these requirements is to add the advective term only in the liquid phases, which then leads to a normal advection in pure liquid-liquid interfaces and is only modified through $\mathscr{L}$ in the presence of additional solid phases [37]. This results in the phase-field equations

$$\tau(\varphi)\varepsilon\left(\frac{\partial\varphi_\alpha}{\partial t} + \mathbf{u}\cdot\nabla\varphi_\alpha\right) = -\frac{\delta\mathscr{F}}{\delta\varphi_\alpha} - \mathscr{L}. \qquad (7)$$

The fluid velocity $\mathbf{u}$ is interpolated as $\mathbf{u} = \varphi_l\mathbf{u}_l + \varphi_s\mathbf{u}_s$. Here, $\mathbf{u}_l$ and $\mathbf{u}_s$ are the fluid velocities in the solid phases (intermetallic and substrate) and the fluid phases (droplet and surrounding), respectively. In the solid phases, the fluid velocity $\mathbf{u}_s$ is assumed to be zero and hence the fluid velocity is rewritten as $\mathbf{u} = \varphi_l\mathbf{u}_l$, where φ_l is defined as $\varphi_l = \varphi\cdot\boldsymbol{l}$, with $l_\alpha = 0$ for $\alpha = $ S, I and $l_\alpha = 1$ for $\alpha = $ L, V. According to Ref. [37] which is based on Ref. [38], the fluid velocity is governed the following momentum balance equation

$$\rho(\varphi)\left(\frac{\partial\mathbf{u}}{\partial t} + \mathbf{u}\cdot\nabla\mathbf{u}\right) = -\varphi_l\nabla p + \nabla\cdot\eta(\varphi)\left(\nabla\mathbf{u} + \nabla\mathbf{u}^T\right) + \mathbf{f}_{\text{cap}} - \mathbf{M}_l^d. \qquad (8)$$

Here, $\rho(\varphi)$ and $\eta(\varphi)$ are the density and viscosity, respectively, which are interpolated by the corresponding properties of the individual phases, namely, $1/\rho = \sum_\alpha(1/\rho_\alpha)\varphi_\alpha$ and $1/\eta = \sum_\alpha(1/\eta_\alpha)\varphi_\alpha$. p is the pressure and $\mathbf{M}_l^d := \underline{\mathbf{T}}\cdot\nabla\varphi_l$ is a dissipative interfacial stress term which is used to achieve the no-slip boundary condition at the solid-liquid interface. Here, $\underline{\mathbf{T}}$ is the averaged viscous stress tensor which is approximated as $\underline{\mathbf{T}} = h\eta(1 - \varphi_l)\mathbf{u}_l\otimes\mathbf{n}/\lambda$, with λ and h being the interfacial width and a friction coefficient, respectively (see Refs. [37,38] for the details). $\mathbf{f}_{\text{cap}}$ is the capillary force acting on the surface which may be modeled in a conservative manner

$$\mathbf{f}_{\text{cap}} = -\nabla\cdot\underline{\boldsymbol{\Theta}}, \qquad (9)$$

where the capillary tensor is chosen to be

$$\underline{\underline{\Theta}} = \sum_{\alpha < \beta} \sum_{\beta} \gamma_{\alpha\beta} \varepsilon \left(\mathbf{q}_{\alpha\beta} \otimes \mathbf{q}_{\alpha\beta} - \tfrac{1}{2} \mathbf{q}_{\alpha\beta}^2 \mathbf{I} \right), \quad \text{with} \quad \mathbf{q}_{\alpha\beta} = \varphi_\alpha \nabla \varphi_\beta - \varphi_\beta \nabla \varphi_\alpha,$$

such that $\mathbf{f}_{cap}$ is consistent with the capillary force $\sigma_{\alpha\beta}\kappa_{\alpha\beta}\mathbf{n}$ in the description of sharp interface, where $\kappa_{\alpha\beta}$ and $\mathbf{n}$ is the mean curvature and normal vector of the α-β interface.

The density and the viscosity of the liquid droplet are, respectively, described by a linear expression [46].

$$\rho_L = \rho_L^0 + \rho_T(T - T_L), \tag{10}$$

and by the Arrhenius equation [46].

$$\eta_L = \eta_\infty \exp\left(\frac{E_A}{R_g T}\right). \tag{11}$$

The functional expressions of the temperature dependence of these quantities for different compositions have been experimentally measured and the results are reported in Ref. [46]. The coefficients, ρ_L^0, ρ_T, T_L, η_∞ and E_A in Eqs. (10) and (11) are determined by fitting the experimental data.

The phase-field equations, Eqs. (6)–(8) are discretized on a mesh with a size of $200d_0 \times 200d_0$ in 2D and $150d_0 \times 150d_0 \times 100d_0$ in 3D by using the finite difference method, where d_0 is the capillary length of the system and is determined as [47] $d_0 = \frac{\gamma_{LI} v_m}{R_g T \Delta c^2} \approx 0.57$ nm. The upwind differencing scheme is used for the convective part. In order to have stable numerical simulations, a dynamic time step [48].

$$\Delta t \leq \frac{2}{5} \left\{ \frac{1}{2} \text{Re} \left(\frac{1}{\Delta x^2} + \frac{1}{\Delta y^2} + \frac{1}{\Delta z^2} \right), \frac{\Delta x}{|u_{max}|}, \frac{\Delta y}{|v_{max}|}, \frac{\Delta z}{|w_{max}|} \right\} \tag{12}$$

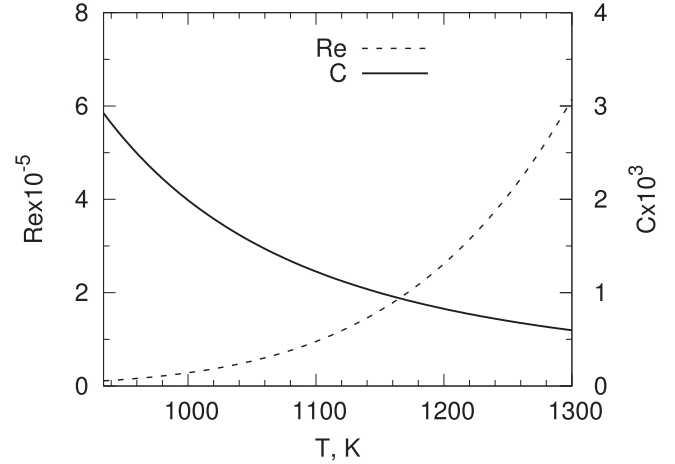has been used, where Re is the Reynolds number, Δx, Δy and Δz are

Fig. 2. The dimensionless numbers Re and C as a function of temperature, based on the experimental data for the density and the viscosity. Here, the Reynolds number Re, which is a reflection of the viscous force relative to inertial force, is defined as $Re = \rho_L d_0 u_0 / \eta_L$, where the characteristic velocity u_0 is expressed as D_{Al}/d_0. The temperature dependent density ρ_L and viscosity η_L are taken from the experimental data [46] and the diffusivity D_{Al} as a function of temperature is from Ref. [49]. The dimensionless number $C = \frac{R_g T}{v_m} \frac{d_0^2}{\rho_L D_{Al}^2}$ measures the strength of the capillary force relative to diffusion.

the discretized spatial step in the x, y and z dimension, respectively, and u_{max}, v_{max} and w_{max} are the maximal velocities in the x, y and z direction, respectively.

In order to resolve the capillary length, the spatial step for the discretization is set as $\Delta x = \Delta y = \Delta z = d_0$ and the diffuse interface has a width of $12d_0$ by setting $\varepsilon = 5d_0$. So, the size of the droplet which can be simulated by the phase-field model is restricted by

Table 1
Parameters for the phase-field simulation.

Parameter	Description	Value	Reference
d_0	Capillary length	$5.7365 \cdot 10^{-10}$ m	
v_m	Molar volume	$1.1 \cdot 10^{-5}$ m³/mol	
R_g	Universal gas constant	8.31 J/(mol K)	
k_b	Boltzmann constant	$8.617 \cdot 10^{-5}$ eV/K	
D_i^V, D_i^L	Diffusivity in vapor and liquid	$1.91 \cdot 10^{-7} \cdot \exp\left(\frac{-0.28 \text{ eV}}{k_b T}\right)$ m²/s	[49]
D_i^I, D_i^S	Diffusivity in intermetallic and solid	0	
Δx	Discretization spatial step	$5.7365 \cdot 10^{-10}$ m	
Δy	Discretization spatial step	$5.7365 \cdot 10^{-10}$ m	
Δz	Discretization spatial step	$5.7365 \cdot 10^{-10}$ m	
Δt	Discretization time step	Eq. (12)	[48]
τ	Relaxation coefficient	5.96×10^7 J/(m⁴s)	
ε	Interfacial width parameter	2.87×10^{-9} m	
$N_x \times N_y$	Simulation domain size in 2D	114.73×114.73 nm²	
$N_x \times N_y \times N_z$	Simulation domain size in 3D	$86.05 \times 86.05 \times 86.05$ nm³	
γ_{SL}	Surface tension of S-L	1.8874 J/m²	[5]
γ_{SV}	Surface tension of S-V	1.2813 J/m²	[5]
γ_{LV}	Surface tension of L-V	1.0769 J/m²	[5]
γ_{IV}	Surface tension of I-V	1.15 J/m²	[5]
γ_{SI}	Surface tension of S-I	0.4 J/m²	[5]
γ_{LI}	Surface tension of L-I	$0.1 \sim 1.4$ J/m²	
$\gamma_{\alpha\beta\delta}$	Higher order term for suppressing third phases	30 J/m²	
ΔE_{Au-Au}	Bond energy of Au-Au	221.3 kJ/mol	[50]
ΔE_{Al-Al}	Bond energy of Al-Al	186 kJ/mol	[50]
ΔE_{Al-Au}	Bond energy of Al-Au	326 kJ/mol	[50]
ρ_L^0	Parameter for liquid density	2.29 g/cm³	[46]
ρ_T	Parameter for liquid density	-2.51 g/(cm³ K)	[46]
T_L	Parameter for liquid density	934 K	[46]
η_∞	Parameter for liquid viscosity	0.214 mPa s	[46]
E_A	Parameter for liquid viscosity	14.3 kJ/mol	[46]
a_0	Lattice constant	404.96 pm	[52]

the capillary length, the spatial step of the discretization and the diffuse interface width. For parallel computing, the simulation domain is divided into several sub-domains with the technique of Message Passing Interface (MPI). For the capillary length of $d_0 = 0.57$ nm, the present computation capacity allows to simulate droplets on the scale up to micrometers. Because of high computational effort for computing fluid dynamics and in order to save some computation time, the radius of the droplet is set on the scale of nanometers in our phase-field simulations. In addition, as shown in the supplemental materials, the size of the simulation domain has a minor effect on the simulation results.

Two dimensionless numbers are used to characterize the capillary flow. One is the Reynolds number Re which is defined as $\text{Re} = \frac{\rho_L d_0 u_0}{\eta_L}$ and is an evaluation of the viscosity force relative to the inertial force. Here, the characteristic velocity u_0 is defined as $u_0 := D_{Al}/d_0$, where the temperature dependent expression for the self-diffusion coefficient of Al referring to Ref. [49] is shown in Table 1. The second dimensionless number is defined as $C = \frac{R_g T}{v_m} \frac{d_0^2}{\rho_L D_{Al}^2}$, which is a reflection of the strength of the capillary force relative to diffusion. The two dimensionless numbers as a function of temperature are shown in Fig. 2.

As depicted in Ref. [5], the surface tensions of S-L, S-V, L-V and I-V are estimated by a nearest neighbor bond-breaking model

$$\gamma_{ij} = \frac{1}{2} \times \frac{\Delta E}{0.5 Z N_A} \times k \times \frac{N}{A}, \tag{13}$$

where ΔE is the bond energy as shown in Ref. [50] and tabulated in Table 1, Z is a coordination number and we have $Z = 12$ for face centered cubic (fcc) crystals of Al and Au, and N_A is the Avogadro constant. The number of bonds in one mole crystal is $0.5 Z N_A$ and the energy per bond writes $\Delta E/0.5 Z N_A$. The parameter k denotes the number of broken bonds per atom. For a fcc structure, each atom in a (111) surface is connected to 9 atoms and there are 3 dangling bonds. Thus, to create two (111) surfaces, 3 bonds per atom on average has to be broken [51]. The ratio N/A measures the number of atoms per area. For fcc crystals in the (111) plane, the number of atoms per area is expressed as $N/A = \frac{4}{\sqrt{3}a_0^2}$ [51], where a_0 is the lattice constant [52]. The factor $1/2$ in Eq. (13) refers to half the work to break a bond apportioned to that atom and the other half of the surface energy addresses the other side of the bond.

The bond energies of Au-Au, Al-Al and Al-Au are used to calculate the surface energies of solid-vapor γ_{SV}, liquid-vapor γ_{LV} and solid-liquid γ_{SL}. The bond energy in the intermetallic phase Al$_2$Au has not been tabulated in literature and is supposed to be calculated by the weighted mean value: $(2\Delta E_{Al-Al} + \Delta E_{Au-Au})/3$, resulting in a surface tension of $\gamma_{IV} = 1.15$ J/m^2. The surface tensions of liquid-intermetallic and solid-intermetallic are parameters to computationally explore the influence on the phase transition and microstructure formation process. The surface tensions as well as other parameters for the phase-field simulation are shown in Table 1.

3. A general concept based on a four-phase-three-component system

In the current study, we consider four phases: an Al-rich liquid phase, an Au-rich solid phase, an intermetallic Al$_2$Au phase and the surrounding-vapor phase. In order to model the evolution of such a four-phase system, a ternary Al-Au-X phase diagram has been constructed by an extension of the binary Al-Au phase diagram [36]. Here, X represents the main component of the surrounding-vapor phase.

The free energy densities for the liquid, solid and vapor phases are formulated as the ideal solution model

$$f^\alpha(\mathbf{c}^\alpha, T) = \sum_{j=1}^{3} \left(c_j^\alpha G_j^\alpha + R_g T c_j^\alpha \ln c_j^\alpha \right), \tag{14}$$

where c_1^α, c_2^α and c_3^α are the mole fractions of Au, Al and X in phase α, $\alpha = $ S, L, V, and G_1^α, G_2^α and G_3^α are constants to be determined. The free energy density of the intermetallic phase is chosen to be a regular solution form considering only the interaction between Al and Au

$$f^I\left(\mathbf{c}^I, T\right) = \sum_{j=1}^{3} \left(c_j^I G_j^I + R_g T c_j^I \ln c_j^I \right) + \omega c_1^I c_2^I, \tag{15}$$

where ω, G_1^I, G_2^I and G_3^I are coefficients to be determined.

Applying the strategy and the following condition from Ref. [5].

$$\partial_{c_1^L} f^L = \partial_{c_1^S} f^S, \tag{16}$$

$$\partial_{c_2^L} f^L = \partial_{c_2^S} f^S, \tag{17}$$

$$f^L - \partial_{c_1^L} f^L c_1^L - \partial_{c_2^L} f^L c_2^L = f^S - \partial_{c_1^S} f^S c_1^S - \partial_{c_2^S} f^S c_2^S. \tag{18}$$

we obtain a ternary phase diagram of Al-Au-X for four phases: liquid, solid, intermetallics and vapor, as shown in Fig. 3. The ternary phase diagram inherits one important feature of the binary Al-Au phase diagram. The equilibrium mole fractions of Al and Au at the phase boundary $c_X = 0$ coincide with the binary phase diagram. When the mole fraction of X tends to zero, the equilibrium mole fractions of Au in liquid and solid are higher than that in liquid and intermetallic phases. Due to this property, the solid substrate dissolves into the liquid phase with time when an Al-droplet is placed on top of an Au-solid substrate.
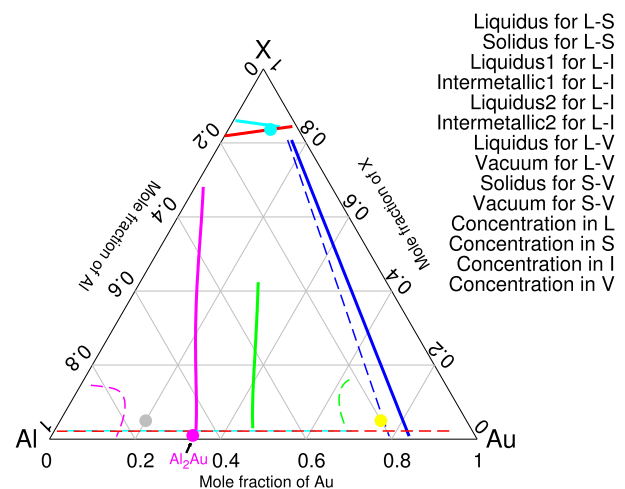

Fig. 3. Assessed ternary phase diagram at a dimensionless temperature of $T/T_m = 1.2$: solid and dashed blue lines denote the equilibrium mole fractions of Al, Au and X in liquid and solid phases considering the thermodynamic equilibrium between solid and liquid. The other lines are interpreted analogously according to the legends. The circle points indicate the initial concentration for the phase-field simulations. The constructed diagram is adapted from our previous work [5] and is presented here for a better understanding of the current work. (For interpretation of the references to color in this figure legend, the reader is referred to the Web version of this article.)

4. Simulation results and discussion

4.1. The evolution of the intermetallic Al₂Au phase in the process of reactive wetting

At the beginning, a nucleus of the intermetallic Al₂Au phase is placed at the liquid-solid interface. The mole fractions of Au, Al and X in the L, S, I and V phases are set as (0.2, 0.7, 0.1), (0.7, 0.2, 0.1), (0.33, 0.66, 0.01), (0.0988, 0.065, 0.8362), respectively, as indicated by the circles in Fig. 3. The mole fraction of X in the solid and liquid phases is set as 0.1, which seems to be a qualitative value. On the one hand, the realistic solubility of Au and Al in the vapor phase has not been tabulated in literature and the quantitative values are hard to be addressed. On the other hand, the present study focuses on the growth of the intermetallic phase due to the reaction between the solid and liquid phases, rather than the phase transition with the vapor phase. The non-zero mole fraction of X in the solid, liquid and intermetallic phases is set only to capture the phase boundaries of S-V, L-V and I-V. Despite the mole fraction of X being qualitative, these settings give rise to phase equilibria between the vapor phase and the other phases to ensure that there is no phase transition taking place at the interfaces of S-V, L-V and I-V. Also, the capillary flow instead of diffusion dominates the evolution of the interfaces of S-V, L-V and I-V and thus, the qualitative setting of the concentration of X does not affect the simulation results. In addition, the equilibrium contact angle is solely determined by the corresponding surface tensions rather the concentration. We note that the concentrations of X in the solid and liquid phases have been set within the order of 0.1 and the concentrations of the metal elements in the vapor phase are on the order of 0.01 in the work of Villanueva [8].

Fig. 4 illustrates the time evolution of the intermetallic phase for a surface tension of $\gamma_{LI} = 0.6$ J/m². The temporal evolution of the intermetallic phase is quantified by measuring the contact angle θ as a function of time, as depicted in Fig. 4(a). We see that the angle θ rapidly decreases with time and, after reaching a minimum value of about $10°$, it gradually increases with time. After a certain time ($tD_{Al}/d_0^2 > 100$), the angle θ does not change significantly with time, maintaining a constant value of $35°$. According to the evolution behavior of the angle, we divide the θ-t diagram into two stages: S1 and S2, which are separated by the vertical dashed line.

The evolution of the angle θ shown in Fig. 4(a) is comprehended by analyzing the corresponding microstructure evolution. In stage S1, the nucleus, which is represented by the orange phase in Fig. 4(b), spreads in the horizontal direction due to the surface tension relation, $\gamma_{SL} > \gamma_{SI} + \gamma_{LI}$. In the spreading process, the angle θ rapidly decreases with time to wet the solid-liquid interface in order to reduce the total surface energy. Because of the surface tension relation, it is impossible for the intermetallic phase to stay inside the droplet. With time, provided that the volume of the intermetallic phase is sufficient, the intermetallic layer moves
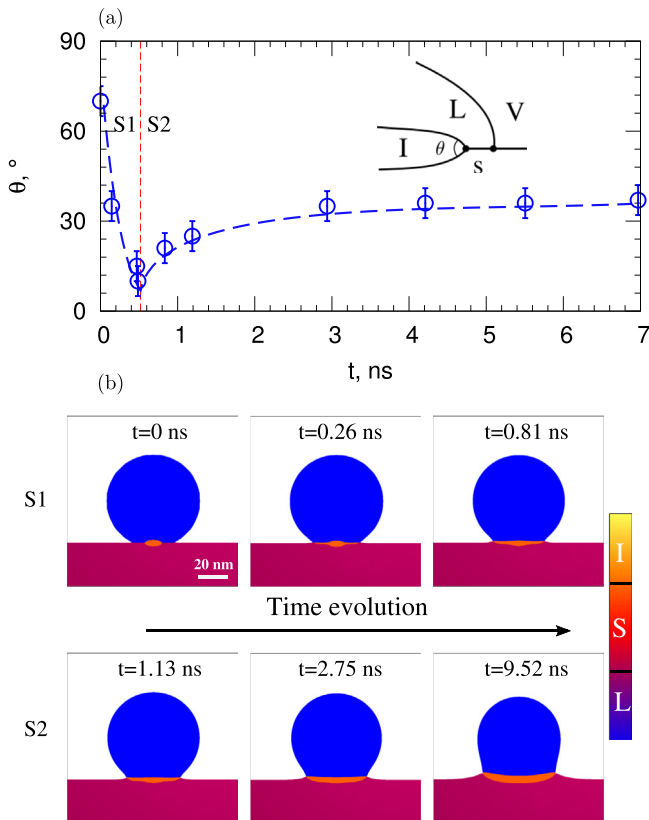

Fig. 4. Phase-field simulations of reactive wetting in 2D without fluid dynamics for $\gamma_{LI} = 0.6$ J/m²: (a) The angle θ (see the inset) between the upper and lower interfaces of the intermetallic phase as a function of time, where the temporal evolution is divided into two stages S1 and S2. (b) The time evolution of the microstructures during the stages S1 and S2. Here, different phases are characterized by the phase-field order parameter, as indicated by the color bar. (For interpretation of the references to color in this figure legend, the reader is referred to the Web version of this article.)
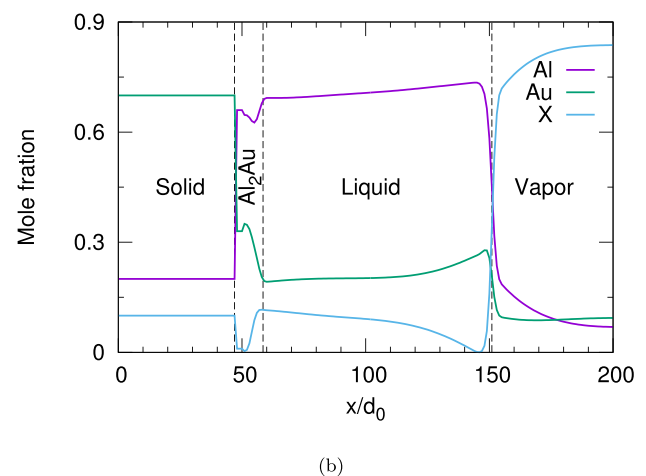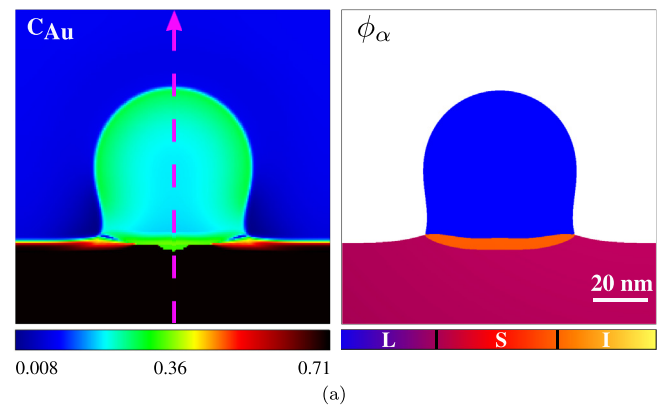

Fig. 5. The distribution of the concentration of Al, Au and X and the phase-field order parameter at a simulation time of 9.72 ns for $\gamma_{LI} = 0.6$ J/m² without fluid dynamics: (a) Contour plot of the concentration distribution of Au (left image) and the index of the phase-field (right image). (b) Distribution of Au, Al and X along the magenta dashed line marked in (a).

outside the Al-droplet and approaches direct contact with the vapor phase. Thereafter, two triple junctions, L-I-V and S-I-V are established and the evolution of the contact angle enters stage S2. In this stage, the angle θ gradually increases with time to fulfill the force balance condition at the two triple junctions, until it reaches the equilibrium value of about $35°$.

The dynamic behavior for the intermetallic phase, either inside or outside the droplet, is very hard to capture by real experiments because of the non-transparency of the alloy system. So, it is difficult to quantitatively compare the simulation results with experiments. However, qualitatively similar microstructures have been observed in experiments [53], where the intermetallic layer is in contact with the surrounding phase and two triple junctions are formed (see Fig. 1(e)). It is necessary to emphasize that both, the contact angle at the triple points as well as the resulting microstructure are significantly affected by the surface tension of γ_{LI}, the effect of which will be addressed in section 4.2.

Fig. 5(a) portrays the distribution of the concentration of Au and the phase-field order parameter at a simulation time of 9.72 ns for $\gamma_{LI} = 0.6$ J/m^2. The distributions of the species Au, Al and X along the vertical dashed line are displayed in Fig. 5(b). The concentration of Au varies from 0.7 to 0.2 across the intermetallic Al$_2$Au layer from the solid phase to the liquid phase. It is noted that the concentration ratio of Al to Au is about 2 in the intermetallic phase and that there is a concentration gradient in the bulk of the intermetallic phase. Due to the concentration gradient, the intermetallic phase grows in the vertical direction and its thickness increases with time. Because of the phase transition, the volumes of the solid and liquid phase both are consumed with time, in contrast to the inert wetting, where the volumes of the phases are conserved.

4.2. Effect of the surface tension γ_{LI} on the growth of the intermetallic layer

In the process of reactive wetting, the concentrations in the liquid and intermetallic phases do not necessarily remain constant and may vary with time due to diffusion and reaction. From the Gibbs adsorption relation, we know that the surface tension depends on the interfacial concentration. So, the surface tension may not be a constant value during reactive wetting. The dependence of the surface tension on the concentration is expressed as $d\gamma = \Gamma dc$ [54], where Γ is the surface excess coefficient. Since the coefficient Γ for the Al-Au system has not been tabulated in literature, we do not change the surface tension of γ_{LI} with time for simplicity, but

aim to investigate how the microstructures are affected by different constant surface tensions.

Fig. 6 shows the effect of the surface tension γ_{LI} on the growth of the intermetallic layer. Fig. 6(a)-(d) correspond to the microstructures at the same simulation time of 15.74 ns, where the contact angle has already reached steady-state. For $\gamma_{LI} = 0.1$ J/m^2 and $\gamma_{LI} = 0.6$ J/m^2, as depicted in Fig. 6(a) and (b), respectively, the intermetallic phase spreads in the horizontal direction and finally is in contact with the vapor phase. In these two cases, two triple junctions, L-I-V and S-I-V are formed. The contact angle at the triple junction can be estimated according to the rule of Neumann's triangle. With an increase of the surface tension γ_{LI} to 1.0 J/m^2, a quadruple junction is temporally formed, as illustrated in Fig. 6(c). This value of surface tension indicates a morphological transition from spreading to engulfment of the intermetallic phase. A further increase in the surface tension γ_{LI} gives rise to a different scenario, as portrayed in Fig. 6(d), where the growth of the intermetallic phase in the horizontal as well as the vertical direction has been significantly suppressed. In contrast to the cases in Fig. 6(a), (b) and (c), the intermetallic phase locates inside the primary liquid droplet accompanied by triple junctions of L-I-V and S-L-V.

To further explore the growth of the intermetallic phase in the process of reactive wetting, we measure the change of the angle θ with time and the results are presented in Fig. 6(e). We observe that for $\gamma_{LI} = 0.1$, 0.6 and 1.0 J/m^2, the angle first decreases and then increases with time after passing through a minimum, similar to the observation in Fig. 4. Before reaching the minimal value, the decreasing rate of the angle is higher for a smaller surface tension of γ_{LI}. This is due to the fact that the driving force for the spreading of the intermetallic layer is expressed as $\gamma_{LS} - (\gamma_{SI} + \gamma_{LI})$ and increases with a decrease of the surface tension of γ_{LI}. After passing through the minimal value, the intermetallic phase is in contact with the surrounding vapor phase. In this stage, the angle increases with time and converges to different values depending on the surface tension of γ_{LI}. For a higher surface tension of $\gamma_{LI} = 1.4$ J/m^2, the contact angle monotonically decreases with time and reaches an equilibrium value of $35°$ without passing through an obvious minimum, as depicted by the solid orange circles. There is a slight increase of the angle from $32°$ to $35°$ from the time 7 ns–9 ns. This slight change of the contact angle is due to the non-synchronized evolution rate of the L-I and S-I interfaces for the formation of the equilibrium angle. The L-I interface evolves much faster that the S-I interface because of a higher Gibbs-Thomson coefficient as a result of a larger surface
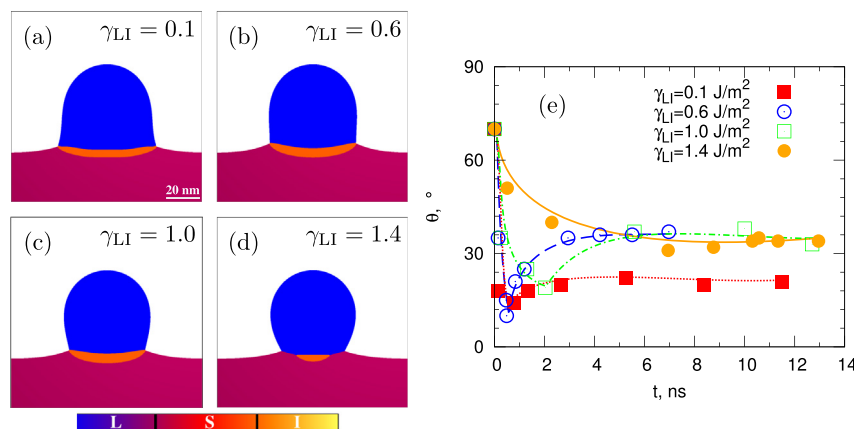

Fig. 6. Effect of the surface tension γ_{LI} on the growth of the intermetallic layer without fluid dynamics: (a), (b), (c) and (d) correspond to the microstructures at a simulation time of 15.74 ns for $\gamma_{LI} = 0.1$ J/m^2, $\gamma_{LI} = 0.6$ J/m^2, $\gamma_{LI} = 1.0$ J/m^2, and $\gamma_{LI} = 1.4$ J/m^2, respectively. (e) shows the contact angle θ as a function of time for different surface tensions γ_{LI}. The square and circular symbols stand for the simulation results and the lines are used to guide the eye. Here, the definition of the angle θ is referred to Fig. 4(a).

tension. When the L-I interface is almost flat because of the larger surface tension, the S-I interface is still moving into the solid phase to open the angle between the L-I and S-I interface, in order to fulfill the Neumann's condition at the S-L-I triple junction.

We remark that the liquid-intermetallic interfacial tension is very hard to experimentally measure. Also, it should be noted that the apparent contact angle, which is experimentally determined to estimate the corresponding surface tension, is not the direct contact angle between the liquid and solid phases (see section 4.3), because of the formation of the intermetallic layer in between the Al-liquid and Au-substrate. Hence, one should be careful when using the measured apparent contact angle to evaluate the surface tension. In addition, we know that the interfacial tension changes with concentration for a fixed temperature. So, the distinct simulated microstructures for different surface tensions of γ_{LI} may correspond to the cases of different compositions. If the concentration changes with time, the surface tension also varies with time. In most cases, the surface excess coefficient Γ is positive [54,55] and the surface tension increases with time with an increase of the concentration. For such a dynamic surface tension, we expect the following transition for the microstructures: Movement of the S-I-L triple junction towards the S-L-V triple junction → Formation of the S-I-V and L-I-V triple junctions (Fig. 6(a)) → Degeneration of the S-I-V and L-I-V triple junctions due to the increase of the surface tension → Reestablishment of the S-I-V and L-I-V triple junctions (Fig. 6(d)). Moreover, the parametric studies for the surface tension effect on the formation of the intermetallic compound in this section may provide guidance for industry applications, such as how the microstructure is affected by adjusting the surface tension, which can be achieved, for example, by adding a small amount of a third element.

4.3. Effect of capillary flow on the spreading of the droplet and the growth of the intermetallic phase

As shown in the introduction section, the evolution of the contact angle in the reactive wetting process follows the expression: $\vartheta - \vartheta_e \sim \exp(-t/\chi)$. Previous phase-field simulations [29] have been devoted to investigate the dynamic contact angle but the formation of the intermetallic phase is not considered. Sessile droplet experiments [23] have shown that the occurrence of the intermetallic phase results in the breakup of the S-L-V triple junction into S-I-V and L-I-V junctions. Thus, the final equilibrium contact angle as well as the dynamics is expected to be affected by the intermetallic phase. Although intermetallic phases have been incorporated in the phase-field studies in Ref. [8], it lacks comparative studies for the dynamic contact angle with and without intermetallic phase, and, therefore, how the spreading and the final equilibrium angle ϑ_e is affected by the formation of the intermetallic phase has not yet been revealed. Moreover, the natural capillary flow has a significant effect on the spreading of the droplet [8]. In contrast to our previous work [5] where capillary flow is not considered, we herein present comparative studies with and without capillary flow.

In this section, we consider four different setups: (i) without capillary flow and with intermetallic phase, (ii) with capillary flow and with intermetallic phase, (iii) without capillary flow and without intermetallic phase, and (iv) with capillary flow and without intermetallic phase. The effect of capillary flow on the spreading of the droplet as well as on the growth of the intermetallic phase is explored by comparing the time evolution of the contact angle in the considered four scenarios.

Fig. 7(a) illustrates the time evolution of the apparent contact angle for the cases (i)-(iv). Here, the contact angle ϑ refers to the
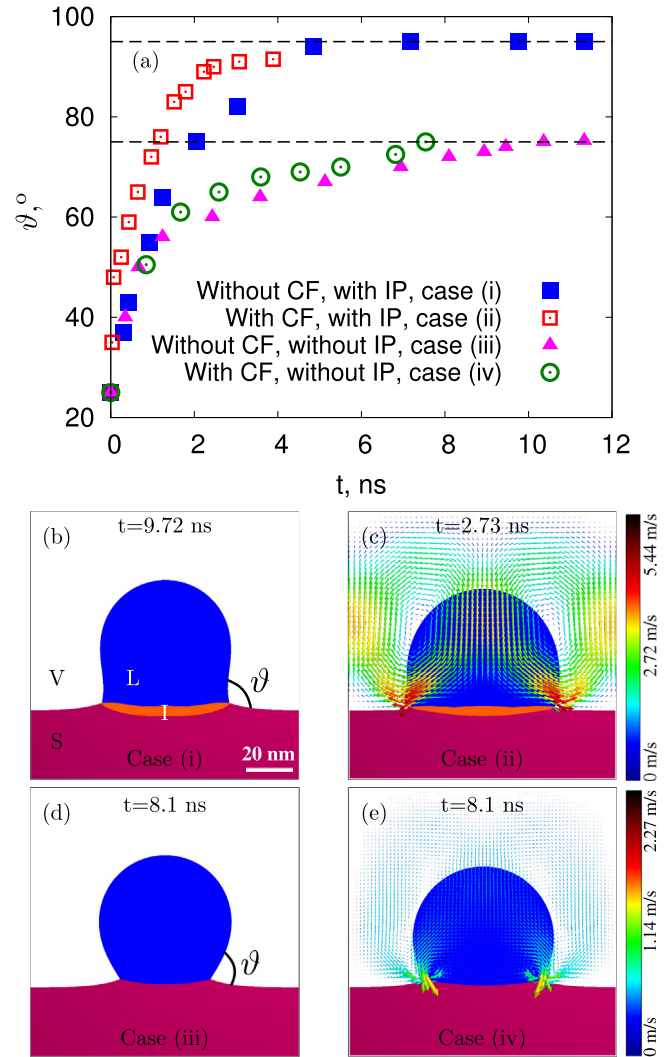

Fig. 7. Effect of capillary flow and of the formation of the intermetallic phase on the temporal evolution of the microstructures: (a) Time evolution of the apparent contact angle ϑ (see (b) and (d) for the illustration of ϑ) for four different scenarios: (i) Without capillary flow (CF) and with intermetallic phase (IP), (ii) with CF and with IP, (iii) without CF and without IP, and (iv) with CF and without IP. (b)–(d) illustrate the microstructures for cases (i)-(iv), respectively, where the angle ϑ has reached its equilibrium value. The arrows in (c) and (e) depict the vector field for the convection and the values of the fluid velocity are referred to the corresponding color bars. Here, we set $\gamma_{LI} = 0.1$ J/m^2 when the intermetallic phase is present. For computing the capillary flow, the dimensionless number is set as $C = R_g T d_0^2/(v_m \rho_L D_{Al}^2) = 1000$. (For interpretation of the references to color in this figure legend, the reader is referred to the Web version of this article.)

exterior angle between the liquid phase and the substrate, independent from the presence of the intermetallic phase, as illustrated in Fig. 7(b) and (d). It is noted that the angle ϑ is different from the angle θ between the upper and lower interfaces of the intermetallic phase as indicated in Fig. 4. We see that in all cases, the contact angle ϑ exponentially converges to constant values. This kind of exponential evolution of the contact angle is consistent with previous experimental works [21,22]. The difference is that the contact angle converges to a value of around 95° in cases (i) and (ii), and to a value of about 75° in cases (iii) and (iv).

The different values of the converged angles in Fig. 7(a) can be well understood by analyzing the corresponding microstructures which are displayed in Fig. 7(b)–(e). The microstructures including the intermetallic Al$_2$Au phase without and with capillary flow at a
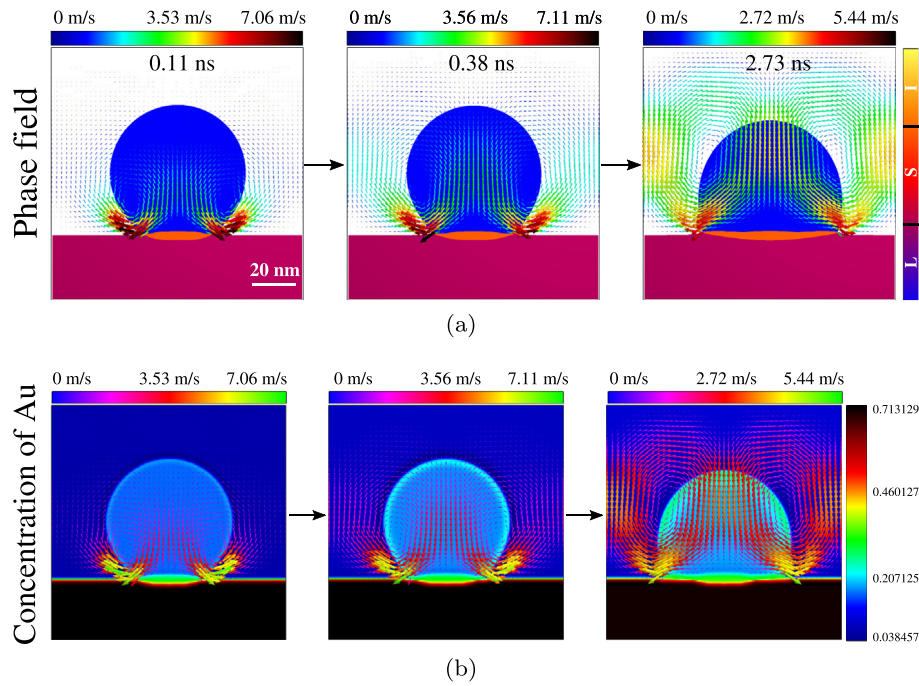
Fig. 8. Temporal change of the phase field φ_α (a) and the concentration of Au (b), corresponding to the simulation setup in Fig. 7(c). Here, the arrows stand for the convection vectors of the capillary flow and the values for the velocity are referred to the color bars at the top of each figure. The color legends for the phase field and the concentration are shown at the right hand side of the images. The simulation time in (b) for the concentration is the same as in (a) for the phase field. (For interpretation of the references to color in this figure legend, the reader is referred to the Web version of this article.)

simulation time of 9.72 ns and 2.73 ns are illustrated in Fig. 7(b) and (c), respectively. The simulation results for cases (iii) and (iv) are shown in Fig. 7(d) and (e), respectively. As can be seen from the figures, with the consideration of the intermetallic phase, the liquid phase and the substrate are not in direct contact with each other and the final contact angle ϑ_e is therefore not determined by the equilibrium condition at the S-L-V triple junction. So, the converging angle of 95° in cases (i) and (ii) is a result of the equilibrium condition at the two triple points of S-I-V and L-I-V. Contrarily, the equilibrium angle of 75° in cases (iii) and (iv) is fixed by the force balance at the S-L-V triple junction. Another observation in Fig. 7(a) is that the rate of convergence in the case with capillary flow is faster than in the case without capillary flow since the mass transfer in the former case consists of diffusion and convection, and in the latter case is only caused by diffusion.

A closer comparison between Fig. 7(b) and (c) reveals that the intermetallic layer at the converged states of the contact angle is thinner when capillary flow is considered. The inhibition effect of

the capillary flow on the thickness of the intermetallic phase is due to the following two factors: (i) The first factor is the difference in the time scales of diffusion and convection. As shown in Fig. 7(a), the convergence of the contact angle due to convection takes less time than for pure diffusion. In both cases, with and without capillary flow, the growth of the intermetallic phase is dominated by diffusion. So, when the capillary flow is considered, the intermetallic layer has less time for the diffusion-dominated growth and the corresponding evolution seems to be inhibited. (ii) The second factor is the convection of the capillary flow. The time evolution of the intermetallic phase with capillary flow (C = 1000) for the phase field is illustrated in Fig. 8(a). The corresponding temporal evolution of the concentration of Au in Fig. 8(b) shows that the Au species is convected from the bulk of the droplet to the triple point to enhance the kinetics near the region of the triple junction. Hence, the Au-component is accumulated near the triple junction and is reduced at the L-I interface. Regarding the fact that the predominant diffusant for the growth of the intermetallic phase is Au [9],
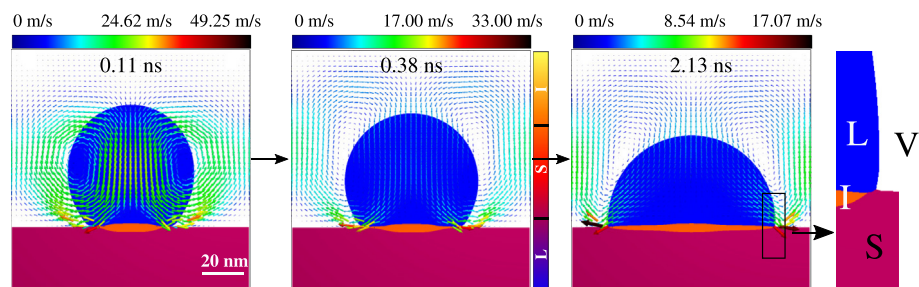

Fig. 9. Time evolution of the phase field and the convection field of the capillary flow for a stronger capillarity with C = 10000. The legend for the phase field is shown at the right hand side of the second image. The arrows in the first three figures represent the vectors for the capillary flow and the values of the velocity are indicated by the color legends at the top of each figure. The right most figure illustrates a magnification of the S-I-L and S-V-L triple junctions. (For interpretation of the references to color in this figure legend, the reader is referred to the Web version of this article.)

the reduction of the Au-component at the L-I interface gives rise to a slow kinetic for the intermetallic layer.

A further increase of capillary flow by artificially increasing C to 10000 results in a stronger inhibition effect for the growth of the intermetallic phase. This effect can be see in Fig. 9. The motion of the S-L-V triple junction at the initial state is driven by the capillary flow, whereas the movement of the S-I-L triple point is due to diffusion. Increasing the capillary flow accelerates the spreading speed of the S-L-V triple junction and may lead to a microstructure where the S-I-L triple point stays behind the S-L-V triple junction, as shown by the third image and the magnified figure in Fig. 9. Though the S-I-L triple point is not stable according to Young's law, triple points of S-V-I and L-V-I cannot be established since the volume of the intermetallic phase is not sufficient large to

completely wet the S-L interface. Also, from the experimental data, the dimensionless number C (see Fig. 2) cannot reach a value of 10000, which is assumed for the study in Fig. 9. So, the microstructure in Fig. 9 is unlikely to be observed in experiments. However, we learn from Fig. 9 that the intermetallic phase can be greatly suppressed in the lateral as well as the vertical direction by increasing the capillary effect.

4.4. 3D simulation

In this section, we present selected three-dimensional simulations for the reactive wetting. To reduce the computational time, half of the configuration is considered in a simulation domain of $150d_0 \times 150d_0 \times 100d_0$ and the complete setup containing a full droplet is reconstructed according to the axis-symmetrical property. The purpose of this section is to reveal different evolution behavior of the contact angle in 2D and 3D, and also to explore the 3D microstructures with and without capillary flow.

Fig. 10 compares the different evolution behaviors of the contact angle ϑ in 2D and 3D. The time evolution of the contact angle ϑ for a surface tension $\gamma_{LI} = 0.6$ J/m^2 without capillary flow is shown in Fig. 10(a). From the comparison, the evolution rate of the contact
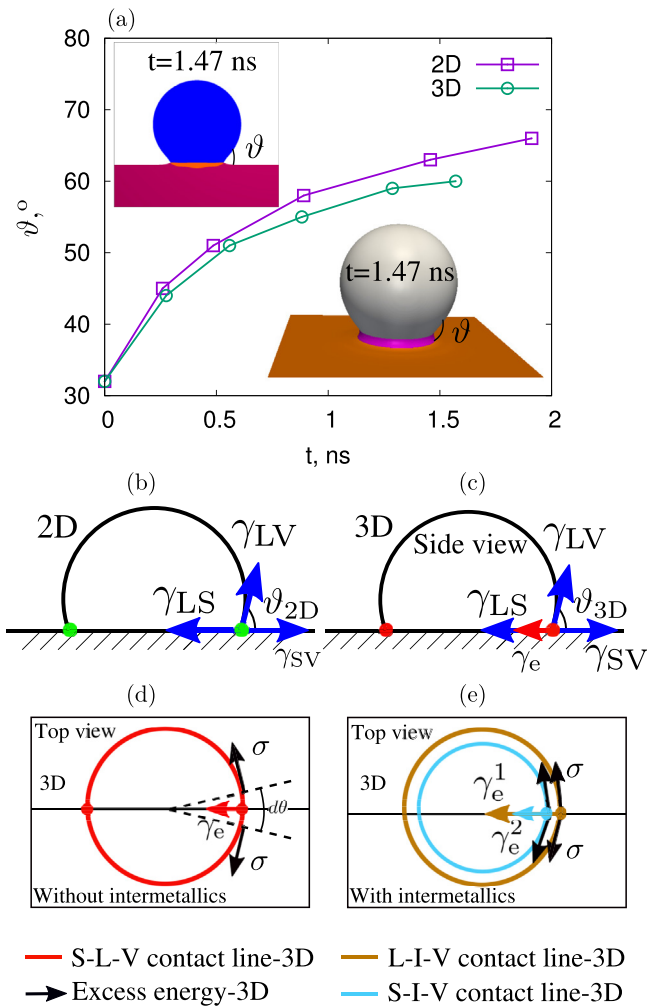

Fig. 10. Different evolution behavior of the contact angle ϑ in 2D and 3D for $\gamma_{LI} = 0.6$ J/m^2 without capillary flow: (a) illustrates the temporal evolution of the contact angle ϑ in 2D and 3D from the phase-field simulations. The upper and lower insets are the microstructures in 2D and 3D, respectively, at the same simulation time of 1.47 ns. (b) shows the analytical calculation of the contact angle for a S-L-V triple junction in 2D: $\cos\vartheta_{2D} = (\gamma_{SV} - \gamma_{LS})/\gamma_{LV}$, following Young's law. In contrast, the contact angle in 3D is estimated as $\cos\vartheta_{3D} = (\gamma_{SV} - \gamma_{LS} - \gamma_e)/\gamma_{LV}$, where γ_e is an additional tension (red arrow) due to the increase of the dimensionality. (d) explains the reason for the appearance of γ_e. The triple junctions in 2D (green points) transform to a triple line (the red circle) which has a tension σ. Geometric analysis shows that the line tension σ has an inward contribution, as indicated by the red arrows in (c) and (d), to the force balance at the S-L-V triple junction. The scenario with two triple lines of S-I-V and L-I-V when the intermetallic phase is present is depicted in (e). (For interpretation of the references to color in this figure legend, the reader is referred to the Web version of this article.)
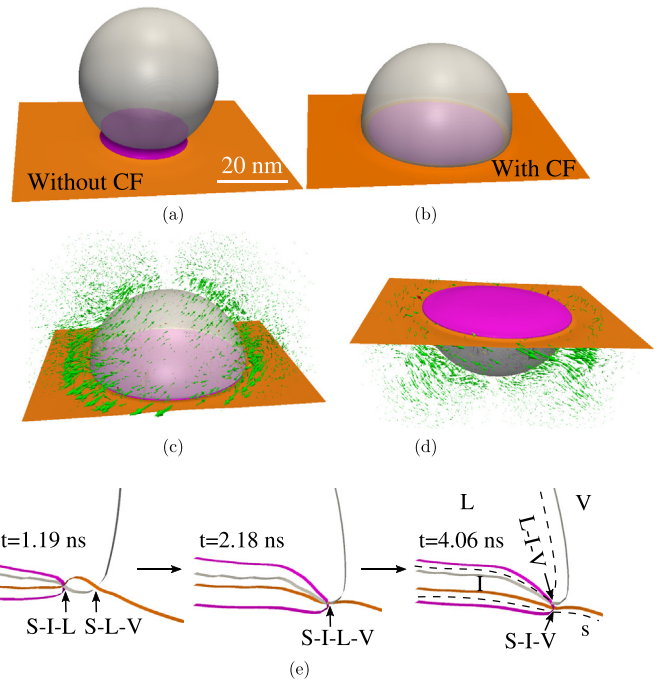

Fig. 11. Reactive wetting incorporating the growth of the intermetallic phase in three dimensions for $\gamma_{LI} = 0.1$ J/m^2: (a) and (b) depict the microstructures without and with capillary flow (CF) at the same simulation time of 1.34 ns. In the former case, the triple lines of S-I-V and L-I-V are established, whereas in the latter case, the intermetallic phase is inside the droplet. The comparison shows that the liquid phase spreads faster in the latter case and the growth of the intermetallic phase is relatively inhibited. (c) and (d) are the top and bottom views of the microstructure with CF (C = 1000) at a simulation time of 2.32 ns, where triple lines of S-I-V and L-I-V are formed. Here, the green arrows stand for the vector field of the convection. (e) shows the transition of S-I-L and S-L-V triple junctions into a S-L-I-V quadruple junction and the dissociation of the S-L-I-V quadruple junction into S-I-V and L-I-V triple junctions with CF from the phase-field simulations. In the first and last images, the gray, magenta and orange lines correspond to the isolines of $\varphi_L = 1/3$, $\varphi_I = 1/3$ and $\varphi_S = 1/3$, respectively. The intersection points correspond to the triple junctions. It is noted that the interface is located at $\varphi_i = 1/2$ as shown by the dashed line at the right most case. The isolines of $\varphi_i = 1/4$ for different phases are shown in the second image, where the quadruple junction is given by the locus of $\varphi_S = \varphi_L = \varphi_I = \varphi_V = 1/4$. (For interpretation of the references to color in this figure legend, the reader is referred to the Web version of this article.)

angle in 3D is slower than that in 2D and the angle in 3D is smaller than the one in 2D at the same considered time. For a S-L-V triple junction, the equilibrium contact angle in 2D is given by $\cos\vartheta_{2D} = (\gamma_{LS} - \gamma_{SV})/\gamma_{LV}$, as shown in Fig. 10(b) following Young's law. In contrast, the following interpretation shows that the contact angle in 3D is given by $\cos\vartheta_{3D} = (\gamma_{LS} - \gamma_{SV} - \gamma_e)/\gamma_{LV}$, where γ_e is an additional contribution due to the increase of the dimensionality. In contrast to the presence of two triple junctions in 2D, a curved triple line appears in 3D, as shown by the red circle in Fig. 10(d). According to Ref. [56], the curved contact line has a tension σ, which has a unit of J/m. Considering the force balance on an infinitesimal arc with a length of $d\theta R$ along the triple line on the plane parallel to the substrate, the tension σ has the contribution: $2\sigma\sin(d\theta/2) \approx \sigma d\theta$, in the inward radial direction, as illustrated in Fig. 10(d). Here, $d\theta$ is an infinitesimal angle and R is the base radius of the contact line. The contribution $\sigma d\theta$ by the length of the arc $d\theta R$ yields a tension per unit length: $\gamma_e := \sigma/R$ (unit: J/m^2, the same unit as surface tension), as illustrated by the red arrow in Fig. 10(d). This additional contribution changes the force balance at the S-L-V triple junction, as depicted in Fig. 10(c). When the intermetallic phase is present, two contact lines of L-I-V and S-I-V appear (Fig. 10(e)) and the contact angle is affected by the third dimensional contributions: γ_e^1 and γ_e^2. Because of this contribution, the driving force in 3D is reduced and the convergence rate is consequently decreased. It should be emphasized that the contribution γ_e has a dependence on the base radius of the droplet and, therefore, the contact angle in 3D is also affected by the size of the droplet, which is consistent with the experimental report [57].

Fig. 11(a) and (b) show the 3D microstructures at the same time of 1.34 ns without and with capillary flow, respectively. In the former case, triple lines of S-I-V and L-I-V are established, whereas in the latter case, the intermetallic phase is inside the droplet. The comparison reveals that the droplet spreads faster and the growth of the intermetallic phase is inhibited when capillary flow is taken into account, similar to the observations in Figs. 7 and 9. In the case with capillary flow, the intermetallic phase moves outside the droplet with time and triple lines of S-I-V and L-I-V are formed. Fig. 11(c) and (d) portray the top and bottom views of the microstructures with S-I-V and L-I-V triple lines including the convection field at a simulation time of 2.32 ns. In all cases with and without capillary flow in 2D and 3D, the quadruple junction S-L-I-V is a transient state and dissociates into two triple junctions. The dissociation process when capillary flow is considered is shown in Fig. 11(e). The dissociation can be explained by the criteria proposed by Cahn et al. [58] (see Ref. [5] and the references therein).

5. Conclusion

In summary, by taking Al-Au as an exemplary system and by using a phase-field approach incorporating diffusion mechanisms, we have explored the complex reactive wetting process involving phase transition and fluid dynamics. Differing from our previous work [5], the following new achievements have been obtained in the present work: (i) The wettability of the system is enhanced because of the formation of the intermetallic phase, which can be seen by the comparative studies for the contact angle with and without intermetallic phase in Fig. 7. The wettability can also be improved by decreasing the surface tension γ_{LI}, similar to the finding in Ref. [8]. (ii) The phase-field studies show that the contact angle between the upper and lower interfaces of the intermetallic phase exhibits a non-monotonic growth behavior, as shown in Fig. 4. (iii) A geometric interpretation as well as comparative studies for the 2D and 3D reactive wetting reveals that the contact angle in 3D is determined not only by the surface tensions but also

by the so-called line tension as well as the curvature. The geometric analysis shown in Fig. 10 has not been presented before. (iv) The growth of the intermetallic phase is inhibited by increasing the capillarity.

We remark that in the reactive wetting process, there are two time scales. One is related to diffusion and is relevant for the motion of the S-I-L triple junction as well as for the growth of the intermetallic phase. Also, at the beginning state when the droplet is directly in contact with the solid-substrate, the Au-substrate dissolves into the liquid-droplet by diffusion. The second time scale is set by the capillary flow, which is responsible for the movement of S-L-V and L-I-V triple points and enhances the kinetics of the corresponding triple junctions.

An emphasis in the reactive wetting process is the instance that the solid-substrate is not in direct contact with the droplet after the complete covering of the intermetallic layer at the S-L interface. In this scenario, it makes no sense to apply the Young's law: $\cos\vartheta = (\gamma_{SV} - \gamma_{SL})/\gamma_{LV}$, neither to evaluate the contact angle nor to estimate the surface tension according to the observed angle. The Young's equation might be used to calculate the contact angle between the solid and liquid phases, if the S-L-V triple junction is dominated by the capillarity and the contact angle reaches a temporary equilibrium value prior to the formation of the S-I-V and L-I-V triple points. But it should be noted that this equilibrium state is transient. A more comprehensive study on the transient state has to rely on more precise thermodynamic and kinetic database, such as surface tensions and diffusivities.

Another vital parameter which has not been explored in the present work is the interfacial kinetic coefficient, which is related to the phase-field modeling parameter $\tau(\varphi)$. Presently, we have set a uniform value of $\tau_{\alpha\beta} = 5.96 \cdot 10^7$ J/(m^{4}s) for all the interfaces and the corresponding interfacial kinetic coefficient is in the magnitude of 1 cm/(sK), which is consistent with experimental data for alloy systems [59]. The kinetic coefficient may have two effects on the reactive wetting process: (i) Non-uniform kinetic coefficients can lead to non-synchronized evolution rate of the interfaces. While the faster kinetic interface is already in equilibrium, the lower kinetic interface is still adjusting to the equilibrium state. Therefore, the convergence rate of the contact angle is restricted to the evolution speed of the slower kinetic interface. (ii) The kinetic coefficient impacts the evolution rate of the S-L-I and S-L-V triple junctions. The proceeding rate of the S-L-I triple junction towards the S-L-V triple junction, which is affected by the kinetic coefficients of the two triple junctions, determines the time scale for the convergence of the contact angle. As the phase-field evolution is proportional to γ/τ (see Eq. (7)), increasing the kinetic coefficient has an identical effect as decreasing the surface tension, and hence, enhances the wettability of the system, as demonstrated in Fig. 6. Uniform phase-field mobilities τ have been also used in Ref. [8]. A further study using inhomogeneous phase-field mobilities is demanded.

Appendix A. Supplementary data

Supplementary data related to this article can be found at https://doi.org/10.1016/j.actamat.2017.12.015.

References

[1] G. Kumar, K.N. Prabhu, Review of non-reactive and reactive wetting of liquids

on surfaces, Adv. Colloid Interface Sci. 133 (2007) 61—89.

[2] G. Clatterbaugh, J. Weiner, H. Charles, Gold-Aluminum intermetallics: ball bond shear testing and thin film reaction couple, IEEE Trans. Compon. Packag. Manuf. Technol. 7 (1984) 349—356.

[3] C. Breach, F. Wulff, New observations on intermetallic compound formation in gold ball bonds: general growth patterns and identification of two forms of Au_4Al, Microelectron. Reliab. 44 (2004) 973—981.

[4] R.C. Blish, S. Li, H. Kinoshita, S. Morgan, A.F. Myers, Gold—Aluminum intermetallic formation kinetics, IEEE Trans. Device Mater. Reliab. 7 (2007) 51—63.

[5] F. Wang, B. Nestler, A phase-field study on the formation of the intermetallic Al_2Au phase in the Al—Au system, Acta Mater. 95 (2015) 65—73.

[6] H. Okamoto, Al-Au (aluminum-gold), J. Phase Equilibria Diffusion 26 (2005) 391—393.

[7] H. Xu, C. Liu, V.V. Silberschmidt, S. Pramana, T.J. White, Z. Chen, M. Sivakumar, V. Acoff, A micromechanism study of thermosonic gold wire bonding on aluminum pad, J. Appl. Phys. 108 (2010) 113517.

[8] W. Villanueva, W.J. Boettinger, G.B. McFadden, J.A. Warren, A diffuse-interface model of reactive wetting with intermetallic formation, Acta Mater. 60 (2012) 3799—3814.

[9] C. Xu, T. Sritharan, S. Mhaisalkar, Thin film aluminum—gold interface interactions, Scr. Mater. 56 (2007) 549—552.

[10] F. Wang, A.M. Matz, O. Tschukin, J. Heimann, B.S. Mocker, B. Nestler, and N. Jost, Numerical and experimental investigations on the growth of the intermetallic Mg_2Si phase in Mg infiltrated Si-foams, Adv. Eng. Mater. 1700063.

[11] Y.L. Corcoran, A.H. King, N. de Lanerolle, B. Kim, Grain boundary diffusion and growth of titanium silicide layers on silicon, J. Electron. Mater. 19 (1990) 1177—1183.

[12] L. Xu, Y. Cui, Y. Hao, R. Yang, Growth of intermetallic layer in multi-laminated Ti/Al diffusion couples, Mater. Sci. Eng. A 435 (2006) 638—647.

[13] J. Brillo, Thermophysical properties of multicomponent liquid alloys, Walter de Gruyter GmbH & Co KG (2016) 256—258.

[14] T. Kim, J. Lee, Y. Kim, J.-M. Kim, Z. Yuan, Investigation of the dynamic reactive wetting of Sn-Ag-Cu solder alloys on Ni (P)/Au coated Cu substrates, Mater. Trans. JIM 50 (2009) 2695—2698.

[15] H. Wang, F. Wang, F. Gao, X. Ma, Y. Qian, Reactive wetting of Sn0. 7Cu—xZn lead-free solders on Cu substrate, J. Alloy. Comp. 433 (2007) 302—305.

[16] I.A. Aksay, C.E. Hoge, J.A. Pask, Wetting under chemical equilibrium and nonequilibrium conditions, J. Phys. Chem. 78 (1974) 1178—1183.

[17] V. Laurent, D. Chatain, N. Eustathopoulos, Wettability of SiO_2 and oxidized SiC by aluminum, Mater. Sci. Eng. A 135 (1991) 89—94.

[18] L. Yin, B.T. Murray, S. Su, Y. Sun, Y. Efraim, H. Taitelbaum, T.J. Singler, Reactive wetting in metal—metal systems, J. Phys. Condens. Matter 21 (2009) 464130.

[19] N. Eustathopoulos, Dynamics of wetting in reactive metal/ceramic systems, Acta Mater. 46 (1998) 2319—2327.

[20] J. Chen, M. Gu, F. Pan, Reactive wetting of a metal/ceramic system, J. Mater. Res. 17 (2002) 911—917.

[21] J. Ambrose, M. Nicholas, A. Stoneham, Dynamics of braze spreading, Acta Metall. 40 (1992) 2483—2488.

[22] E. Saiz, C.-W. Hwang, K. Suganuma, A.P. Tomsia, Spreading of Sn-Ag solders on FeNi alloys, Acta Mater. 51 (2003) 3185—3197.

[23] K. Landry, C. Rado, R. Voitovich, N. Eustathopoulos, Mechanisms of reactive wetting: the question of triple line configuration, Acta Mater. 45 (1997) 3079—3085.

[24] B. Nestler, A.A. Wheeler, L. Ratke, C. Stöcker, Phase-field model for solidification of a monotectic alloy with convection, Physica D 141 (2000) 133—154.

[25] B. Nestler, H. Garcke, B. Stinner, Multicomponent alloy solidification: phase-field modeling and simulations, Phys. Rev. E 71 (2005) 041609.

[26] A. Lis, M.S. Park, R. Arroyave, C. Leinenbach, Early stage growth characteristics of Ag_3Sn intermetallic compounds during solid—solid and solid—liquid reactions in the Ag—Sn interlayer system: experiments and simulations, J. Alloy. Comp. 617 (2014) 763—773.

[27] M.S. Park, S.L. Gibbons, R. Arróyave, Phase-field simulations of intermetallic compound evolution in Cu/Sn solder joints under electromigration, Acta Mater. 61 (2013) 7142—7154.

[28] H.S. Udaykumar, L. Mao, Sharp-interface simulation of dendritic solidification of solutions, Int. J. Heat Mass Tran. 45 (2002) 4793—4808.

[29] W. Villanueva, K. Grönhagen, G. Amberg, J. Ågren, Multicomponent and multiphase modeling and simulation of reactive wetting, Phys. Rev. E 77 (2008) 056313.

[30] W. Villanueva, W.J. Boettinger, J.A. Warren, G. Amberg, Effect of phase change

and solute diffusion on spreading on a dissolving substrate, Acta Mater. 57 (2009) 6022—6036.

[31] D. Wheeler, J.A. Warren, W.J. Boettinger, Modeling the early stages of reactive wetting, Phys. Rev. E 82 (2010) 051601.

[32] W. Villanueva, W.J. Boettinger, G.B. McFadden, J.A. Warren, A multicomponent and multiphase model of reactive wetting, in: 7th International Conference on Multiphase Flow, 2010.

[33] K. Asp, J. Ågren, Phase-field simulation of sintering and related phenomena—a vacancy diffusion approach, Acta Mat. 54 (2006) 1241—1248.

[34] F. Wang, A. Choudhury, C. Strassacker, B. Nestler, Spinodal decomposition and droplets entrapment in monotectic solidification, J. Chem. Phys. 137 (2012) 034702.

[35] B. Nestler, M. Selzer, D. Danilov, Phase-field simulations of nuclei and early stage solidification microstructures, J. Phys. Condens. Matter 21 (2009) 464107.

[36] M. Li, C. Li, F. Wang, D. Luo, W. Zhang, Thermodynamic assessment of the Al—Au system, J. Alloy. Comp. 385 (2004) 199—206.

[37] M. Selzer, Mechanische und Strömungsmechanische Topologieoptimierung mit der Phasenfeldmethode, PhD thesis, Karlsruhe Instiitute of Technology, 2014.

[38] C. Beckermann, H.-J. Diepers, I. Steinbach, A. Karma, X. Tong, Modeling melt convection in phase-field simulations of solidification, J. Comput. Phys. 154 (1999) 468.

[39] L.Q. Chen, Phase-field models for microstructure evolution, Annu. Rev. Mater. Res. 32 (2002) 113—140.

[40] W.J. Boettinger, J.A. Warren, C. Beckermann, A. Karma, Phase-field simulation of solidification, Annu. Rev. Mater. Res. 32 (2002) 163—194.

[41] B. Nestler, A. Choudhury, Phase-field modeling of multi-component systems, Curr. Opin. Solid State Mater. Sci. 15 (2011) 93—105.

[42] S.M. Allen, J.W. Cahn, A microscopic theory for antiphase boundary motion and its application to antiphase domain coarsening, Acta Metall. 27 (1979) 1085—1095.

[43] J. Hötzer, O. Tschukin, M. Ben Said, M. Berghoff, M. Jainta, G. Barthelemy, N. Smorchkov, D. Schneider, M. Selzer, B. Nestler, Calibration of a multi-phase field model with quantitative angle measurement, J. Mater. Sci. 51 (2016) 1788—1797.

[44] R. Balluffi, S.M. Allen, W.C. Carter, Kinetics of Materials, John Wiley & Sons, 2005.

[45] L. Onsager, Reciprocal relations in irreversible processes I, Phys. Rev. 37 (1931) 405.

[46] H. Peng, T. Voigtmann, G. Kolland, H. Kobatake, J. Brillo, Structural and dynamical properties of liquid Al-Au alloys, Phys. Rev. B 92 (2015) 184201.

[47] J.S. Langer, Instabilities and pattern formation in crystal growth, Rev. Mod. Phys. 52 (1980) 1.

[48] F. Wang, A. Choudhury, M. Selzer, R. Mukherjee, B. Nestler, Effect of solutal Marangoni convection on motion, coarsening, and coalescence of droplets in a monotectic system, Phys. Rev. E (2012) 066318.

[49] F. Kargl, H. Weis, T. Unruh, A. Meyer, Self-diffusion in liquid aluminium, J. Phys. Condens. Matter 340 (2012) 012077.

[50] J.G. Speight, Lange's Handbook of Chemistry, McGraw-Hill, New York, 2005.

[51] P. Wynblati, Introduction to Interfaces and Diffusion, Conference Proceeding: Materials Issues for Generation IV Systems, Springer, 2008.

[52] V.A. Lubarda, On the effective lattice parameter of binary alloys, Mech. Mater. 35 (2003) 53—68.

[53] J. Brillo, Unpublished work.

[54] R. Defay, I. Prigogine, A. Bellemans, Surface tension and adsorption, Longmans London (1966) 378.

[55] J.W. McBain, R.C. Swain, Measurements of adsorption at the air-water interface by the microtome method, Proc. R. Soc. A 154 (1936) 608—623.

[56] I. Szleifer, B. Widom, Surface tension, line tension, and wetting, Mol. Phys. 75 (1992) 925—943.

[57] A. Checco, P. Guenoun, J. Daillant, Nonlinear dependence of the contact angle of nanodroplets on contact line curvature, Phys. Rev. Lett. 91 (2003) 186101.

[58] J.W. Cahn, E.A. Holm, D.J. Srolovitz, Modeling microstructural evolution in two-dimensional two-phase microstructures, Mater. Sci. Forum 95 (1992) 141—158.

[59] Y.A. Baikov, Y.D. Christyakov, Effective kinetic coefficients for some binary metallic alloys within the small and finite supercooling region, Cryst. Res. Technol. 25 (1990) 171—175.